Structure and Property Relationship in the Mixed-Conducting Sr-Fe-Co-O System*

B. Ma and U. Balachandran
Energy Technology Division, Argonne National Laboratory
Argonne, Illinois 60439

J. P. Hodges, J. D. Jorgensen, and D. J. Miller
Materials Science Division, Argonne National Laboratory
Argonne, Illinois 60439

J. W. Richardson, Jr.
Intense Pulsed Neutron Source, Argonne National Laboratory
Argonne, Illinois 60439

April 1998

For submittal to the American Ceramic Society 100th Annual Meeting & Exposition, Cincinnati, OH, May 3-6, 1998.

*Work at Argonne is supported by the U.S. Department of Energy, Federal Energy Technology Center, under Contract W-31-109-Eng-38.

DISCLAIMER

DISCLAIMER

Portions of this document may be illegible in electronic image products. Images are produced from the best available original document.

STRUCTURE AND PROPERTY RELATIONSHIP IN THE MIXED-CONDUCTING Sr-Fe-Co-O SYSTEM

B. Ma*, U. Balachandran*, J.P. Hodges†, J.D. Jorgensen†, D.J. Miller†, and J.W. Richardson, Jr‡.
*Energy Technology Division, Argonne National Laboratory, Argonne, IL 60439
†Materials Science Division, Argonne National Laboratory, Argonne, IL 60439
‡Intense Pulsed Neutron Source, Argonne National Laboratory, Argonne, IL 60439

ABSTRACT

Mixed-conducting ceramic oxides have potential uses in high-temperature electrochemical applications such as solid oxide fuel cells, advanced batteries, sensors, and oxygen-permeable membranes. The Sr-Fe-Co-O system combines high electronic/ionic conductivity with appreciable oxygen permeability at elevated temperatures. Dense ceramic membranes made of this material can be used to separate high-purity oxygen from air without the need for external electrical circuitry, or to partially oxidize methane to produce syngas. Samples of $Sr_2Fe_{3-x}Co_xO_y$ (with $x = 0$, 0.6, 1.0, and 1.4) were prepared by solid-state reaction in atmospheres with various oxygen partial pressures (pO_2) and were characterized by X-ray diffraction, scanning electron microscopy, and electrical conductivity measurements. Phase components of the samples are dependent on cobalt concentration and synthesis pO_2. Total conductivity increases with increasing temperature and cobalt content in the material. Higher ionic transference numbers have been observed in samples with lower cobalt contents. Current-voltage characteristics determined in a gas-tight cell indicate that a bulk effect, rather than a surface exchange effect, is the main limiting factor for oxygen permeation through membranes made of $Sr_2Fe_2CoO_y$. Oxygen permeability measurements at various temperatures showed that oxygen permeability increases with increasing temperature, as expected. At 900°C, an oxygen permeation flux of 2.5 $scc \cdot cm^{-2} \cdot min^{-1}$ was obtained for a $Sr_2Fe_2CoO_y$ disk membrane of 2.9 mm thickness.

INTRODUCTION

Oxides with mixed electronic and ionic conductivities are receiving increased attention because of their applications in high-temperature electrochemical processes [1-5]. For example, they are used as electrodes in solid oxide fuel cells, and if their oxygen permeability is high enough, they can be used as oxygen-separation membranes. Sr-Fe-Co-O has not only high combined electronic and oxygen ionic conductivity but also oxygen permeability that is superior to that of other reported ceramic oxides [6-11]. It is a good candidate material as a dense membrane for the production of high-purity oxygen by gas separation. In an oxygen separation reactor, oxygen can be transported from the high-oxygen-partial-pressure (high-pO_2) side to the low-pO_2 side under the driving force of the pO_2 difference, $\Delta\log(pO_2)$, without the need for external electric circuitry. Balachandran et al. [7] demonstrated that extruded membrane tubes made of Sr-Fe-Co oxide can be used for partial oxidation of methane to produce syngas ($CO + H_2$) in a methane conversion reactor that operates at ≈850°C. In this type of reactor, oxygen on one side of the membrane was separated from air on the other side of the membrane. Methane conversion efficiencies of >98% were observed and the reactor tubes have operated for >1000 h. Moreover, the oxygen flux obtained from the separation of air in this type of conversion reactor is considered commercially feasible. The use of this technology can significantly reduce the cost of oxygen separation [12].

To obtain sufficient oxygen flux, the gas separation reactor must be operated at high temperatures and substantial pO_2 differences. Therefore, stability of the ceramic membranes is an important issue. Certain compounds of $SrFe_{1-x}Co_xO_{3-\delta}$ were found unsuitable for use in gas separation because they lack stability in highly reducing environments [13]. Thermodynamic calculations can normally provide accurate data on the stability of a system. However, specific examples of discrepancies between the calculated thermodynamic stability and experimental results indicate the importance of obtaining supporting data from real systems [14].

In this paper, we report our studies of the crystal structures and transport properties of the $Sr_2Fe_{3-x}Co_xO_y$ materials. Electrical conductivity was determined in atmospheres with various pO_2 levels at elevated temperatures. Oxygen permeability was measured with a gas-tight electrochemical cell. Room-temperature X-ray diffraction (XRD) and scanning electron microscopy (SEM) experiments were also conducted to characterize the material.

SYNTHESIS AND CHARACTERIZATION

The $Sr_2Fe_{3-x}Co_xO_y$ (with x = 0, 0.6, 1.0, and 1.4) powders were made by a solid-state reaction method, with appropriate amounts of $SrCO_3$, $Co(NO_3)_2 \cdot 6H_2O$, and Fe_2O_3. Mixing and grinding were conducted in isopropanol with zirconia media for 10 h. After drying, the mixture was calcined in air at 850°C for 16 h, with intermittent grinding. After final calcination, the powder was ground with an agate mortar and pestle to an average particle size of ~7 μm. The resulting powder was pressed uniaxially with a 1200-MPa load into pellets measuring 21.5 mm in diameter and ~2-5 mm thick. The pellets were then sintered in air at ≈1200°C for 5 h. The true density was measured using a powder sample with an AccuPyc 1330 pycnometer. The bulk density was determined by the Archimedean method, with isopropanol as the liquid medium. The measured density of air-sintered $Sr_2Fe_2CoO_y$ samples was ~95% of the theoretical value. Thin bars ≈1 x 5 x 20 mm^3 were cut from the samples and subjected to post-annealing heat treatments in various low-pO_2 environments at 900-1100°C. The sintered pellets were polished on both sides and used for permeation tests.

Room-temperature X-ray powder diffraction analysis was carried out with a Scintag XDS-2000 diffractometer. Data were taken with Cu K_α radiation. A high-purity intrinsic Ge energy-dispersive detector was used to minimize background due to sample fluorescence. A continuous scan with a 2θ scanning rate of 1°/min and chopping step of 0.03° was used to collect data. SEM observations were conducted with a JEOL JSM-5400 scanning microscope at an accelerating voltage of 20 KeV.

The total conductivity of the sample was determined by the conventional four-probe method, and ionic conductivity was measured with the electron blocking method. Platinum wires were wound onto the specimen bar to serve as current and voltage leads. The resistance of the specimen was measured with an HP 4192A LF impedance analyzer at 23 Hz. Details of the experimental configuration for measuring conductivity were reported in Ref. 10. A K-type thermocouple was attached to an yttria-stabilized zirconia (YSZ) plate on which the sample bars were placed for the heat treatments. The thermocouple was used for both controlling and measuring the temperature of the programmable electric furnace. Temperature uncertainty within the uniform hot zone of the furnace was ±1°C. The desired gaseous environments were obtained by flowing premixed gases through the system.

A schematic diagram of the gas-tight electrochemical cell used in the oxygen permeation experiments is shown in Fig. 1. A sintered pellet of $Sr_2Fe_2CoO_y$ was sealed to a YSZ crucible with Pyrex glass seal. Electrical leads (10-mil Pt wires) were separated from the YSZ crucible and $Sr_2Fe_2CoO_y$ disk membrane by two alumina rings. Electrodes were placed on the bottom and the sidewall of the YSZ crucible. The bottom electrodes were used as pumping electrodes to pump oxygen from the gas-tight cell chamber, whereas the other electrodes were used to determine the pO_2 inside the cell. The pO_2 inside the cell can be determined from the measured electromotive force (EMF), E, generated on the side-wall of the YSZ crucible by

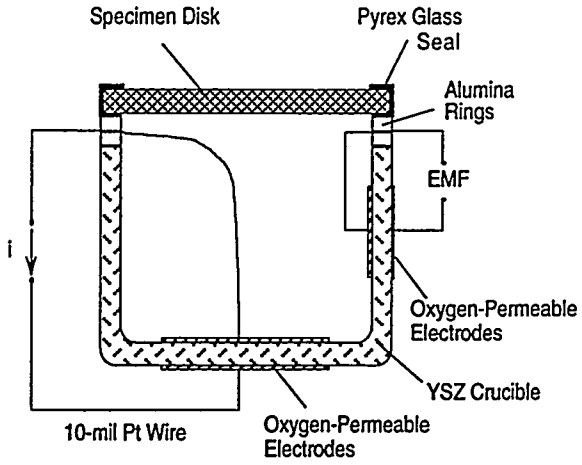

Fig. 1. Schematic drawing of cross-sectional view of gas-tight electrochemical cell used to measure oxygen permeability.

$$pO_2^{II} = pO_2^{I} \exp\left(\frac{4FE}{RT}\right) \qquad (1)$$

where pO_2^{II} and pO_2^{I} are the pO_2 values inside and outside the gas-tight cell, respectively. Other variables are: F, Faraday's constant; R, gas constant; and T, absolute temperature. Reducing oxygen environments were achieved by pumping oxygen out of the gas-tight cell by using the pumping electrodes on the YSZ crucible. Oxygen permeates the $Sr_2Fe_2CoO_y$ disk membrane because of the pO_2 difference on the two sides of the membrane. Under steady-state conditions, the amount of oxygen that enters the cell (by permeating the specimen disk) is equal to that pumped out by the YSZ oxygen pump. Therefore, the flow of oxygen through the specimen can be determined from the current applied to the YSZ oxygen pump. The oxygen permeation flux j_{O_2} (in $mol \cdot cm^{-2} \cdot s^{-1}$) is related to the applied current I (in A) by

$$j_{O_2} = \frac{I}{4FS} \qquad (2)$$

where S is the effective cross-sectional area of the specimen.

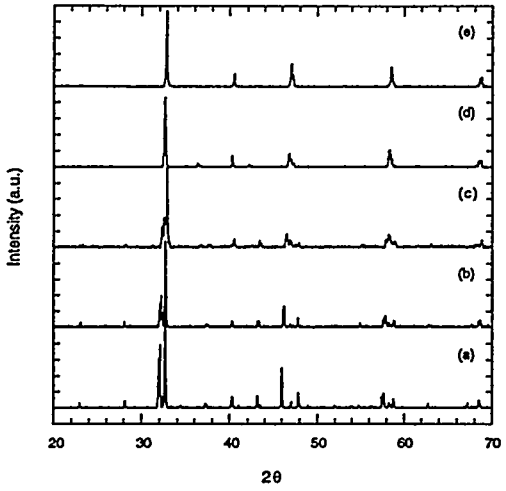

Fig. 2. . Room-temperature X-ray diffraction patterns of air-sintered samples:
(a) $Sr_2Fe_3O_y$, (b) $Sr_2Fe_{2.4}Co_{0.6}O_y$,
(c) $Sr_2Fe_2CoO_y$, (d) $Sr_2Fe_{1.6}Co_{1.4}O_y$,
and (e) $SrFe_{0.8}Co_{0.2}O_y$.

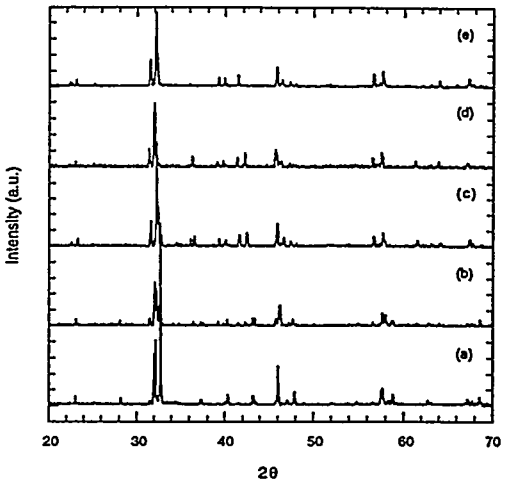

Fig. 3. Room-temperature X-ray diffraction patterns of argonne-sintered samples:
(a) $Sr_2Fe_3O_y$, (b) $Sr_2Fe_{2.4}Co_{0.6}O_y$,
(c) $Sr_2Fe_2CoO_y$, (d) $Sr_2Fe_{1.6}Co_{1.4}O_y$,
and (e) $SrFe_{0.8}Co_{0.2}O_y$.

RESULTS AND DISCUSSION

Room-temperature X-ray diffraction (XRD) patterns of air-sintered $Sr_2Fe_{3-x}Co_xO_y$ are plotted in Fig. 2 for different x values. The powder XRD pattern of the $x = 0$ composition (Fig. 2a) agrees with the result reported for a single-crystal $Sr_4Fe_6O_{13}$ sample [15]. For comparison, the XRD pattern of the perovskite phase $SrFe_{0.8}Co_{0.2}O_{3-\delta}$ is plotted in Fig. 2e. Air-sintered $Sr_2Fe_2CoO_y$ ($x = 1$, Fig. 2c) is a multiple phase material containing ~25% perovskite phase, as obtained from Rietveld analysis [16]. Air-sintered $Sr_2Fe_{2.4}Co_{0.6}O_y$ ($x = 0.6$, Fig. 2b) contains less than 10% perovskite phase, while air-sintered $Sr_2Fe_{1.6}Co_{1.4}O_y$ ($x = 1.4$, Fig. 2d) has more than 90% perovskite phase. Traces of cobalt oxide

impurity phase were also observed in the $Sr_2Fe_{1.6}Co_{1.4}O_y$ sample. XRD patterns of the argon-annealed samples are shown in Fig. 3.

At high temperatures, the perovskite phase can be reduced to the brownmillerite structure [17] in a reducing argon environment ($pO_2 \approx 10^{-6}$ atm). Conversely, argon-annealed $Sr_2Fe_3O_y$ (x = 0, Fig. 3a) has the same structure as that of the air-sintered material and contains no brownmillerite phase, although other argon-annealed cobalt-containing samples all contain an amount brownmillerite phase. The content of the brownmillerite phase in annealed $Sr_2Fe_{3-x}Co_xO_y$ increases with increasing x, as shown in Fig. 3b, 3c, and 3d. The cobalt oxide phase can be seen clearly in the cobalt-containing samples. An XRD of a pure brownmillerite phase of the argon-annealed $SrFe_{0.8}Co_{0.2}O_{3-\delta}$ sample is shown in Fig. 3e for comparison. Analyses of the detailed crystal structure of the $Sr_2Fe_{3-x}Co_xO_y$ samples are in progress. Lattice parameters of the air-sintered materials are listed in Table 1.

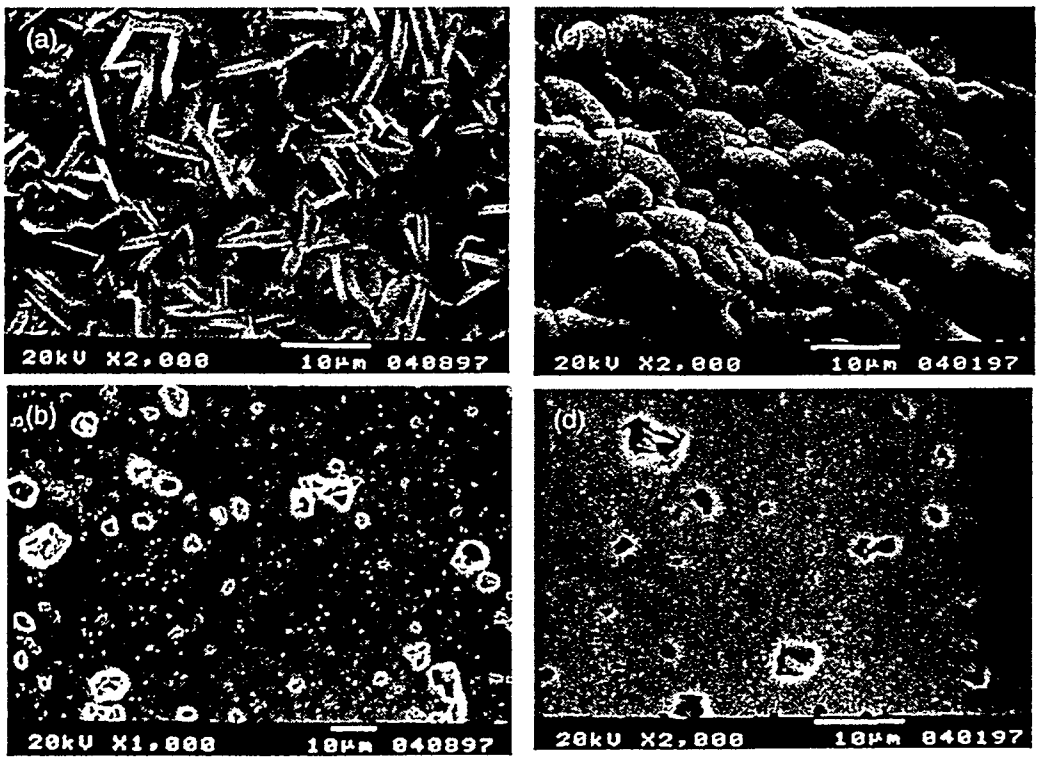

Fig. 4. SEM morphology of $Sr_2Fe_2CoO_x$ sample: (a) original surface of air-sintered sample, (b) polished surface of air-sintered sample, (c) original surface of argon-annealed sample, (d) polished surface of argon-annealed sample.

SEM images of the air-sintered and argon-annealed $Sr_2Fe_2CoO_y$ samples are shown in Fig. 4. They reveal a dense homogeneous structure for both samples. Energy-dispersive X-ray (EDX) elemental analysis showed that the overall atomic ratio of the metal elements is consistent with that in the chemical formula. The polished-surface SEM images showed that the argon-annealed sample is denser and contains fewer pores than the air-sintered sample. A spherical cobalt-rich phase was identified in the argon-annealed sample. By correlating SEM observation with XRD results, we identified the spherical phase as cobalt oxide (CoO, JCPD No. 9-402).

Table 1. Lattice parameters of air-sintered $Sr_2Fe_{3-x}Co_xO_y$ samples

Co content	Phase Components	a (Å)	b (Å)	c (Å)	V (Å^3)
0.0	O (>98%)	11.126	18.978	5.5864	1179.6
0.3	O (>95%) + P (<5%)	11.085	19.016	5.5670	1173.5
0.6	O (>90%) + P (<10%)	11.065	19.008	5.5618	1169.8
1.0*	O (>70%) + P (<25%)	11.017	19.030	5.5463	1162.8

*Contains ~5% CoO phase.

The total conductivity of the $Sr_2Fe_{3-x}Co_xO_y$ sample as a function of temperature is shown in Fig. 5. The conductivity increases as temperature and cobalt content increase. At 900°C, the conductivity of $Sr_2Fe_2CoO_y$ is ~20 and ~6 S·cm^{-1} in flowing air and argon environments, respectively. Conductivities of $Sr_2Fe_{2.4}Co_{0.6}O_y$ and $Sr_2Fe_3O_y$ are ≈10 and ≈0.6 S·cm^{-1}, respectively, at 900°C in air. The ionic transference numbers ($t_{ion} = \sigma_{ion} / \sigma_{total}$) of $Sr_2Fe_2CoO_y$ and $Sr_2Fe_{2.4}Co_{0.6}O_y$ as a function of temperature in air are shown in Fig. 6. The ionic transference numbers for both samples are not strongly

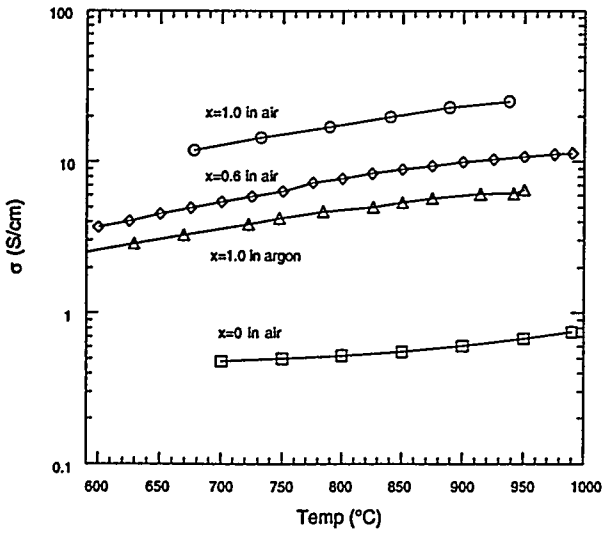

Fig. 5. Temperature dependence of $Sr_2Fe_{3-x}Co_xO_y$ samples.

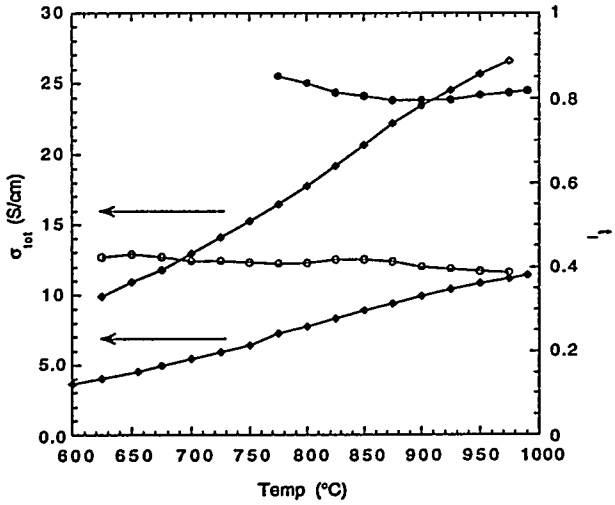

Fig. 6. Temperature dependence of the total conductivity and the ionic transference number of $Sr_2Fe_2CoO_y$ (circles) and $Sr_2Fe_{2.4}Co_{0.6}O_y$ (diamonds).

dependent on temperature. A higher ionic transference number was observed for the sample with lower cobalt content.

For the oxygen permeation experiments, the EMF measured at the sensor electrodes as a function of pumping current at various temperature is plotted in Fig. 7. At a given temperature, the EMF at the sensor electrodes increases with increasing pumping current. EMF increases with decreasing temperature at a given pumping current, and the pumping current increases with increasing temperature to achieve a specific EMF value because the oxygen permeability increases at higher temperatures.

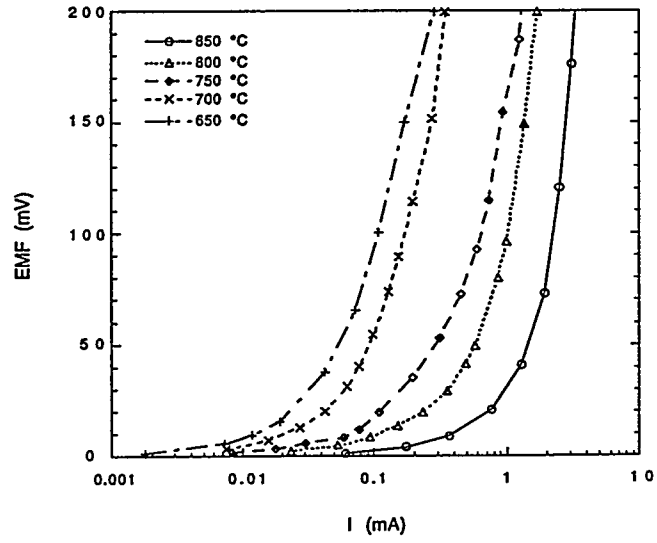

Fig. 7. Electromotive force as a function of pumping current at various temperatures.

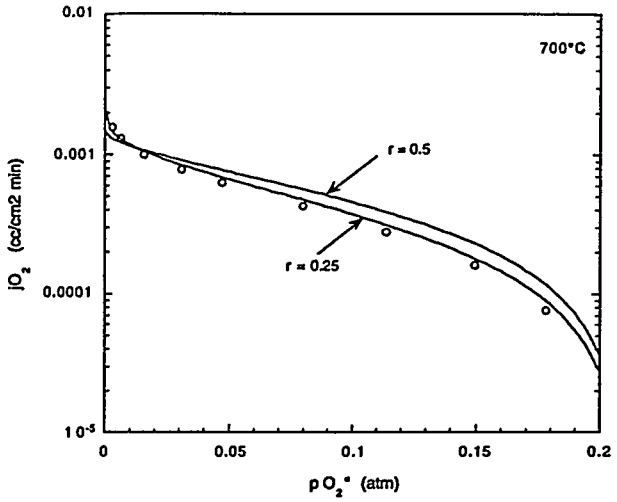

Fig. 8. Steady-state oxygen permeation flux as a function of pO_2 inside the gas-tight cell, and its fitting to Eqs. 3 (r = 0.5) and 4 (r = 0.25).

During our experiment, the gas-tight cell was surrounded by flowing air. The pO_2 inside the cell can be determined by solving Eq. 1. The oxygen permeation flux, j_{O_2}, has been calculated from the steady-state pumping current by solving Eq. 2. To examine the contributions of bulk and interface effects to the oxygen permeation mechanism of the $Sr_2Fe_2CoO_y$ sample, we fit the permeation data with the equation [18]:

$$j_{O_2} = \alpha\left[(pO_2^I)^r - (pO_2^{II})^r\right] \qquad (3)$$

where r is the kinetic order in oxygen of the surface reaction, and a is the exchange rate at pO_2 = 1 atm. For a permeation process where the surface reaction (exchange) effect is the controlling factor, we would have r = 1/2. The surface exchange constant a (in $cm \cdot min^{-1} \cdot atm^{-1/2}$) can be determined by a least-squares fitting of the experimental data.

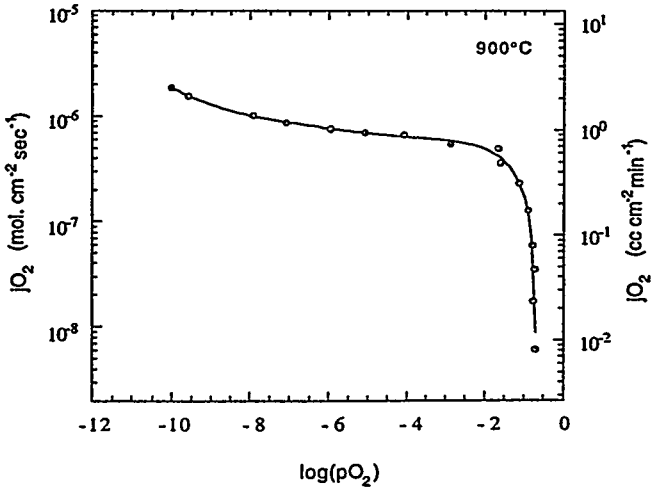

Fig. 9. The pO_2 dependence of steady-state oxygen permeation flux for a 2.9-mm-thick disk membrane.

Where the bulk effect is the controlling factor or, in another words, the surface exchange rate is sufficiently large, the oxygen permeation flux can be defined by [19]:

$$j_{O_2} = \frac{\beta}{L}\left[(pO_2^I)^{1/4} - (pO_2^{II})^{1/4}\right] \qquad (4)$$

where L is the thickness of the membrane (in cm) and b is a bulk diffusion parameter (in $cm^2 \cdot min^{-1} \cdot atm^{-1/4}$). Figure 8 shows typical oxygen permeation data as a function of pO_2 inside the cell, along with the least square-fittings to Eq. 3 (with r = 0.5) and Eq. 4 (with r = 0.25). The fitting is much better to Eq. 4 than to Eq. 3, indicating that bulk diffusion plays the controlling role in the oxygen permeation process in the $Sr_2Fe_2CoO_y$ membrane of ≈1 mm thickness at high temperatures (>650°C).

In Fig. 9, the steady-state oxygen permeation flux of a 2.9-mm-thick pellet specimen at 900°C, determined by solving Eq. 2, is plotted as a function of pO_2 inside the gas-tight cell. Figure 9 shows that j_{O_2} increases dramatically in the range between $pO_2 = 0.21$ and ~10^{-3} atm, and its slope becomes flatter when pO_2 inside the cell is reduced further. Results on oxygen permeability at various pO_2 gradients and temperatures show that, as expected, j_{O_2} increases with temperature and pO_2 gradients. At 900°C, oxygen permeability was ~2.5 $scc \cdot cm^{-2} \cdot min^{-1}$ for a 2.9-mm-thick specimen and increased as membrane thickness decreased.

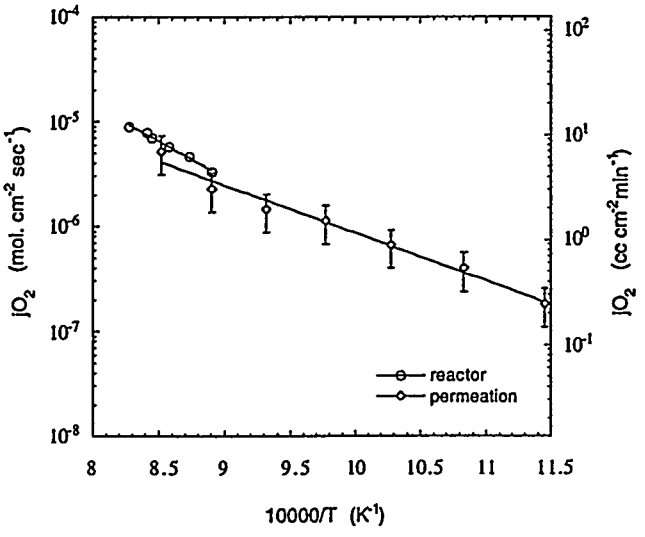

Fig. 10. Temperature dependence of oxygen permeation flux obtained from methane conversion reactor and gas-tight cell.

Sintered thin-wall tubes of $Sr_2Fe_2CoO_y$ were tested in a methane conversion reactor for more than 1000 h [6,7]. An oxygen permeation flux of ~10

$scc \cdot cm^{-2} \cdot min^{-1}$ was observed in a 0.75-mm-thick tubular membrane [6]. Oxygen permeation flux, determined from reactor experiments and with a gas-tight electrochemical cell, have been plotted in Fig. 10 as a function of reciprocal temperature. For comparison, the oxygen permeation flux of the disk membrane was normalized to that of a 0.75-mm-thick membrane. Oxygen permeation data obtained from two independent experiments are in good agreement.

CONCLUSIONS

The phase components of $Sr_2Fe_{3-x}Co_xO_y$ are strongly dependent on cobalt content. The $Sr_2Fe_3O_y$ sample is single-phase material, while the high-cobalt-content samples ($x \geq 0.6$) contain multiple phases. The concentration of a perovskite phase in the high-cobalt-content samples increases with increasing cobalt content. In a reducing argon environment, the single-phase $Sr_2Fe_3O_y$ sample has the same crystal structure as the air-sintered sample, while a brownmillerite phase was observed in the cobalt-containing samples. Cobalt oxide has also been found in the argon-annealed cobalt-containing samples.

The total conductivity of $Sr_2Fe_{3-x}Co_xO_y$ increases with increasing temperature and cobalt content in the sample. At 900°C, the conductivity of $Sr_2Fe_2CoO_y$ in flowing air and argon environments is ~20 and ~6 $S \cdot cm^{-1}$, respectively. The conductivities of $Sr_2Fe_{2.4}Co_{0.6}O_y$ and $Sr_2Fe_3O_y$ are ~10 and ~0.6 $S \cdot cm^{-1}$, respectively, at 900°C in air. The ionic transference numbers do not have a strong dependence on temperature above 600°C in air. A higher total conductivity but lower ionic transference number was observed in the sample with lower cobalt content. The transient conductivity behavior of this sample, after the surrounding atmosphere is switched back and forth, indicates that the phase transition in the materials is reversible.

The oxygen permeation mechanism in the sintered $Sr_2Fe_2CoO_y$ material was found to be bulk controlled. At 900°C, an oxygen permeability of ~2.5 $scc \cdot cm^{-2} \cdot min^{-1}$ was observed in a 2.9-mm-thick membrane. This permeability value agrees with values obtained in the methane conversion reactor experiments.

ACKNOWLEDGMENT

Work at Argonne is supported by the U.S. Department of Energy, Federal Energy Technology Center, under Contract W-31-109-Eng-38.

REFERENCES

1. T. Takahashi and H. Iwahara, *Energy Convers.*, **11**, 105 (1971).
2. B. C. H. Steele, *Mater. Sci. Eng. B-Solid State M.*, **13**, 79 (1992).
3. N. Q. Minh, *J. Am. Ceram. Soc.*, **76**, 563 (1993).
4. R. DiCosimo, J. D. Burrington, and R. K. Grasselli, *J. Catal.*, **102**, 377 (1992).
5. K. R. Kendall, C. Navas, J. K. Thomas, and H.-C. Loye, *Solid State Ionics*, **82**, 215 (1995).
6. U. Balachandran, S. L. Morissette, J. T. Dusek, R. L. Mieville, R. B. Poeppel, M. S. Kleefisch, S. Pei, T. P. Kobylinski, and C. A. Udovich, *Proc. Coal Liquefaction and Gas Conversion Contractor Review Conf.*, S. Rogers et al., eds., **Vol. 1**, pp. 138-160, U.S. Dept. of Energy, Pittsburgh Energy Technology Center (1993).
7. U. Balachandran, T. J. Dusek, S. M. Sweeney, R. B. Poeppel, R. L. Mieville, P. S. Maiya, M. S. Kleefisch, S. Pei, T. P. Kobylinski, C. A. Udovich, and A. C. Bose, *Am. Ceram. Soc. Bull.*, **74**, 71 (1995).
8. Y. Teraoka, H. M. Zhang, S. Furukawa, and N. Yamozoe, *Chem. Lett.*, **1985**, 1734 (1985).
9. Y. Teraoka, T. Nobunaga, and N. Yamazoe, *Chem. Lett.*, **1988**, 503 (1988).
10. B. Ma, J.-H. Park, C. U. Segre, and U. Balachandran, *Mater. Res. Soc. Symp. Proc.*, **393**, 49 (1995).
11. B. Ma, U. Balachandran, C.-C. Chao, J.-H. Park, and C. U. Segre, *Ceram. Trans. Series*, **73**, 169 (1997).
12. U. Balachandran, J. T. Dusek, P. S. Maiya, R. L. Mieville, B. Ma, M. S. Kleefisch, and C. A. Udovich, presented at 11th Intersociety Cryogenic Symp., Energy Week Conf. & Exhibition, Houston, Jan. 28-30, 1997.
13. S. Pei, M. S. Kleefisch, T. P. Kobylinski, J. Faber, C. A. Udovich, V. Zhang-McCoy, B. Dabrowski, U. Balachandran, R. L. Mieville, and R. B. Poeppel, *Catal. Lett.*, **30**, 201 (1995).
14. H. Iwahara, H. Uchida, K. Morimoto, and S. Hosgoi, *J. Appl. Electrochem.*, **19**, 448 (1989).
15. A. Yoshiasa, K. Ueno, F. Kanamaru, and H. Horiuchi, *Mater. Res. Bull.*, **21**, 175 (1986).
16. H. M. Rietveld, *J. Appl. Cryst.*, **2**, 65 (1969).
17. C. Greaves, A. J. Jacobson, B. C. Tofield, and B. E. F. Fender, *Acta Cryst.*, **B31**, 641 (1975).
18. H. J. M. Bouwmeester, H. Kruidhof, A. J. Burggraaf, and P. J. Gellings, *Solid State Ionics*, 53-56, 460 (1992).
19. S. Dou, C. R. Masson, and P. D. Pacey, *J. Electrochem. Soc.*, **132**, 1843 (1985).